Supplementary Information: Field-tunable toroidal moment and anomalous Hall effect in noncollinear antiferromagnetic Weyl semimetal $Co_{1/3}TaS_2$

Pyeongjae Park[1,2], Yoon-Gu Kang[3], Junghyun Kim[1,2], Ki Hoon Lee[4], Han-Jin Noh[5], Myung Joon Han[3*], and Je-Geun Park[1,2,6*]

[1]*Center for Quantum Materials, Seoul National University, Seoul 08826, Republic of Korea*

[2]*Department of Physics & Astronomy, Seoul National University, Seoul 08826, Republic of Korea*

[3]*Department of Physics, KAIST, Daejeon 34141, Republic of Korea*

[4]*Department of Physics, Incheon National University, Incheon, 22012, Republic of Korea*

[5]*Department of Physics, Chonnam National University, Gwangju 61186, Republic of Korea*

[6]*Institute of applied physics, Seoul National University, Seoul 08826, Republic of Korea*

* Corresponding author: jgpark10@snu.ac.kr & mj.han@kaist.ac.kr

Supplementary Notes

Characterization of sample quality in $Co_{1/3}TaS_2$. As intercalated materials have inevitable disorder in general, extensive efforts were given to verifying the quality of the synthesized $Co_{1/3}TaS_2$ samples. We first performed high-resolution powder X-ray diffraction (XRD) and single-crystal XRD, the results of which are shown in Fig. S1 and S2. We observed sharp Bragg peaks without any sizable impurity peaks, which supports the high quality of our sample. In particular, the sharp ($10L$) Bragg peaks (red boxes in Fig. S2b and S2c) indicates the excellent formation of a $\sqrt{3} \times \sqrt{3}$ supercell with homogeneous Co intercalation. Our Rietveld refinement confirms that the samples have identical crystal structures to the previously reported ones [1]. Detailed structural information is shown in TABLE S1 and S2. The quality of the single crystal was further examined by the Raman spectroscopy at 300 K. A sharp peak near 135 cm^{-1} corresponds to the phonon mode dominated by the in-plane motion of Co atoms[2]. Therefore, it supports that the Co atoms are well intercalated into 2H-TaS_2 with negligible disorder.

We also analyzed the composition of Co (x) in Co_xTaS_2 using EDX spectroscopy and inductively coupled plasma atomic emission spectroscopy (ICP-AES) and compared it with the lattice constant c. As shown in TABLE S3, the EDX and ICP-AES results give a consistent x, reasonably close to 1/3. The simple linear relation between x and c (Fig. S4) further implies the validity of x obtained in several samples.

Symmetry analysis and magnetic space groups in $Co_{1/3}TaS_2$. For understanding the origin of the observed AHE, it is crucial to analyze the symmetry of $Co_{1/3}TaS_2$, which belongs to a $P6_322$ space group. It has two-fold rotation symmetry about the a- and a^*-axis (C_{2a} & C_{2a^*}) and 6_3 screw symmetry about the c-axis, i.e., the combination of C_{3z} three-fold rotation and 2_1 screw operation. From the transformation properties of Berry curvature[3], the magnetic symmetry operations of $R = C_{2a}$, C_{2a^*}, TC_{3z}, and $T2_1$ are anti-symmetric with respect to $\Omega_z(R\vec{\mathbf{k}}) \rightarrow -\Omega_z(\vec{\mathbf{k}})$. Therefore, the corresponding AHC component σ_{xy} must be zero due to the Berry curvature cancelation at $\vec{k}$ by $R\vec{k}$ in the Brillouin zone integration. On the other hand, with magnetic symmetries of $R = TC_{2a}$, TC_{2a^*}, C_{3z}, and 2_1, the AHC component σ_{xy} can survive due to their symmetric behavior of $\Omega_z(R\vec{\mathbf{k}}) \rightarrow \Omega_z(\vec{\mathbf{k}})$. Note that out-of-plane magnetization (M_z) is also affected by the same symmetry constraints as σ_{xy} since their transformation properties are identical to each other.

Based on the analysis above, we can identify which one among the six irreducible representations ($\Gamma_1 \sim \Gamma_6$) possess finite σ_{xy} and finite M_z. For example, for the Γ_1 ($P6_322$) spin configuration, in-plane C_2 rotation symmetry enforces σ_{xy} =0 through the anti-symmetry of $\Omega_z(C_2\vec{\mathbf{k}}) \rightarrow -\Omega_z(\vec{\mathbf{k}})$. According to our symmetry analysis, only the Γ_2 and Γ_5 configurations are found to have nonzero σ_{xy} and M_z as observed in our experimental data.

Toroidal moment and model spin Hamiltonian of $Co_{1/3}TaS_2$. As described in the main text, *toroidal dipole moment* ($\mathbf{t} \equiv \sum_i \mathbf{r}_i \times \mathbf{S}_i$) is an essential quantity in explaining the relation between the noncollinear magnetic order and AHE in $Co_{1/3}TaS_2$. Having the linear order of $\mathbf{r}_i$ and $\mathbf{S}_i$, the presence of $\boldsymbol{t}$ breaks both inversion and time-reversal symmetry. Therefore, it usually appears in a chiral lattice magnet[4] or materials with magneto-electric coupling[5]. Since $Co_{1/3}TaS_2$ belongs to the non-centrosymmetric space group $P6_322$, it is natural to introduce such a quantity for this system.

We performed a theoretical analysis with a minimal model Hamiltonian for a microscopic understanding of the observed properties related to the toroidal moment. Two essential features should be realized in the model Hamiltonian. First, the Hamiltonian should reproduce slight out-of-plane canting without a magnetic field. Second, the sign of t_z should be coupled to the direction of the out-of-plane canting, i.e., the $\Gamma_2^{\pm}$ configuration only prefers the canting along the $\pm$z direction. To describe such properties, we suggest the following spin Hamiltonian:

$$H = \sum_{ij} J_{ij}\, \mathbf{S}_i \cdot \mathbf{S}_j \;+\; \sum_{ij} \mathbf{DM}_{ij} \cdot (\mathbf{S}_i \times \mathbf{S}_j) \;+\; K \sum_i S_i^z S_i^\alpha S_i^\beta S_i^\gamma \qquad (1)$$

where i and j is the site index of Co and $S_i^\alpha \equiv \mathbf{S}_i \cdot \hat{\mathbf{n}}_\alpha$ (see Fig. S11a). We only considered nearest-neighbor (NN) intralayer (J_1) and interlayer (J_c) interactions for simplicity. As $Co_{1/3}TaS_2$ is cleavable along the c-axis due to its layered structure, J_1 would be much larger than J_c. Therefore, the large negative Curie-Weiss temperature in $Co_{1/3}TaS_2$ indicates dominant antiferromagnetic J_1, leading to a 120° magnetic ground state. Note that J_c does not contribute to the total energy in such a case, as the effects from the bonds with three inter-layer Co atoms cancel each other out (Fig. 1b).

The second term denotes the DM interaction between NN intralayer and interlayer Co^{2+} ions. DM interaction has been discussed extensively in $TM_{1/3}TaS_2$ due to its crucial role in forming chiral magnetic order. With the 120° spin configuration, however, the in-plane components of the DM vector are permanently canceled out, similar to what happens in J_c. Therefore, the net DM vector points toward the c-axis and only serves as an effective easy-plane anisotropy, stabilizing the 120° spin configuration in the a-b plane. Similarly, symmetric off-diagonal exchange interaction is canceled out, leading to the absence of out-of-plane canting.

We found that the symmetry-allowed higher-order on-site anisotropy can realize the observed weak ferromagnetic moment. A coupling between $S_{x,y}$ and S_z is essential to the link between $\boldsymbol{t}$ and M_z from a phenomenological approach. Therefore, the desired on-site term should contain both in-plane and out-of-plane components of $\mathbf{S}_i$ while obeying the Co's site symmetry: a D_3 point group. The third term in Eq. 1 is such a case, i.e., a product of S_i^z and three in-plane components $S_i^\alpha S_i^\beta S_i^\gamma$, which holds the three-fold rotation symmetry C_{3z} (Fig. S11a). Although the size would be small due to its high order, we found that even $|K|/J_1 \sim 0.02$ is sufficient to induce the observed out-of-plane canting ~$0.01\mu_B$; see Fig. S11c and S11d. Moreover, this term successfully couples the direction of the weak ferromagnetic moment to the direction of t_z, leading to the sign change of AHE by the out-of-plane magnetic field. Note that the sign of K determines whether t_z and M_z are aligned parallel or antiparallel (Fig. S11d).

Crystallographic chiral domain and its relation to the magnetic and transport properties. According to previous studies done on $TM_{1/3}(Ta,Nb)S_2$ (TM = 3d transition metals), single-crystalline $TM_{1/3}(Ta,Nb)S_2$ form hetero-chiral crystallographic domains[6,7]. Therefore, our single-crystalline $Co_{1/3}TaS_2$ is likely to be hetero-chiral as well, which is closely linked to the global alignment of toroidal moments. For a better understanding, we summarized the sign relation between M_z, t_z, and σ_{xy} for each lattice chirality in Table S4. The sign relation between M_z and σ_{xy} was determined by our experimental results (Fig. 2), while the relation between t_z and σ_{xy} was derived from our DFT calculations (Fig. 4f). Note that the DFT calculations were done on the right-handed chiral lattice when we followed the previous study's convention of left/right-handedness[6].

As demonstrated in Table S4, each chiral domain will form a ferro-toroidal ground state (Γ_2) opposite to that of another chiral domain for a fixed canting direction[4]. However, σ_{xy} from each chiral domain does not cancel out each other, as it always follows the sign of M_z, not t_z. In other words, changing chirality will reverse the sign relation between t_z and σ_{xy}. Therefore, the presence of chiral domain does not affect the measurement of σ_{xy}, as far as M_z is uniformly aligned by an out-of-plane magnetic field.

Supplementary Figures

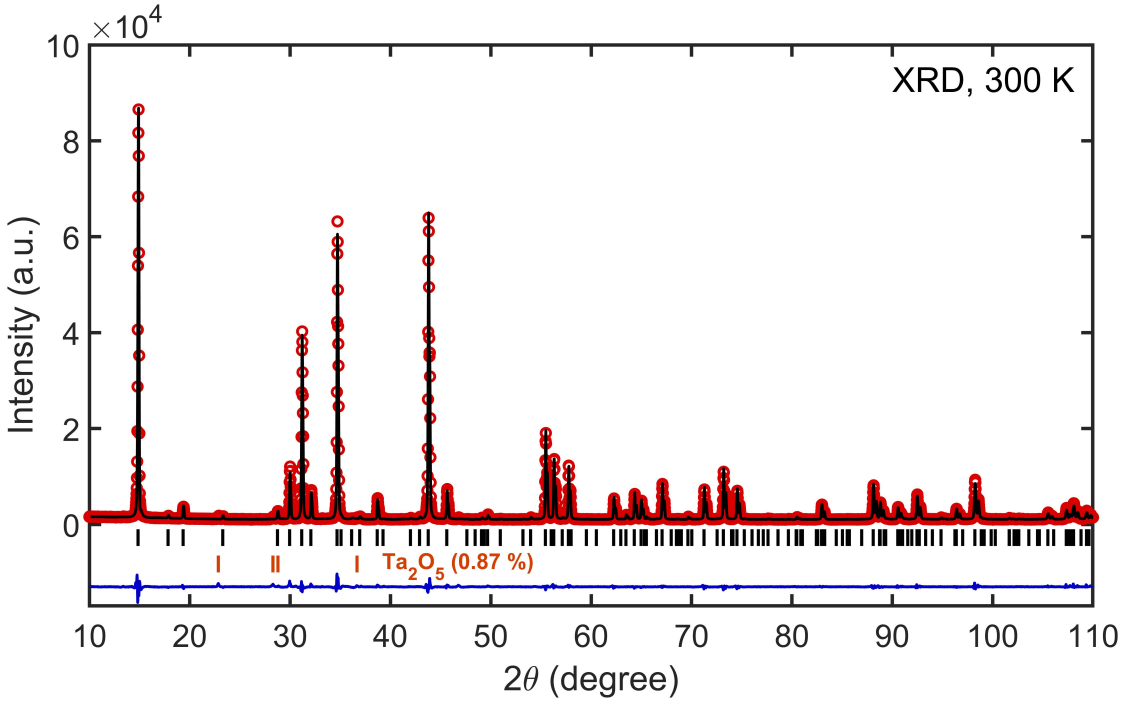

Supplementary Figure 1 | High-resolution powder XRD spectra of $Co_{1/3}TaS_2$ with Rietveld refinement result. Black solid lines show the simulated spectra of the refined crystal structure with the position of Bragg peaks indicated. A solid blue line shows the difference between the data and the simulation. A small amount of the Ta_2O_5 phase was detected, separated by the chemical vapor transport process. Due to the layered crystal structure, we applied the preferred orientation effect in the simulation.

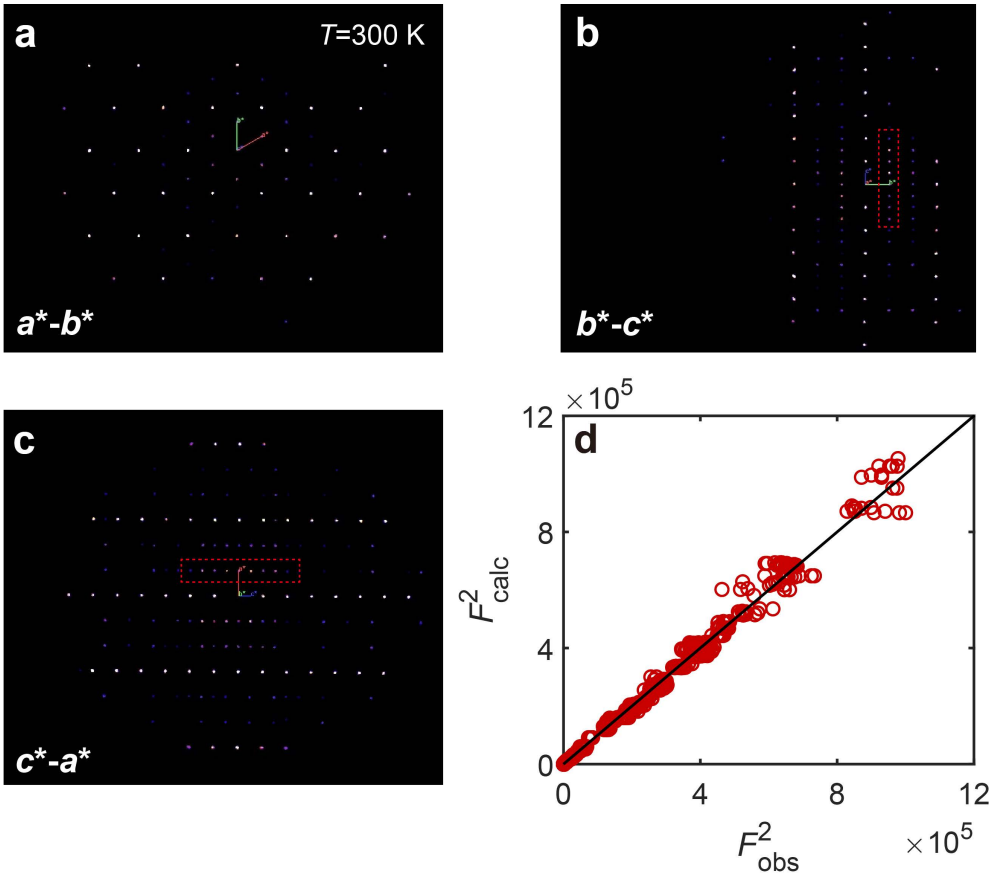

Supplementary Figure 2 | a-c, Measured Bragg peaks of $Co_{1/3}TaS_2$ single-crystal mapped on the a^*-b^*, b^*-c^*, and c^*-a^* planes. **d,** Rietveld refinement result of the measured single-crystal XRD pattern. Red dashed boxes in **b** and **c** indicate (10*L*) Bragg peaks, which correspond to $\sqrt{3} \times \sqrt{3}$ superlattice peaks.

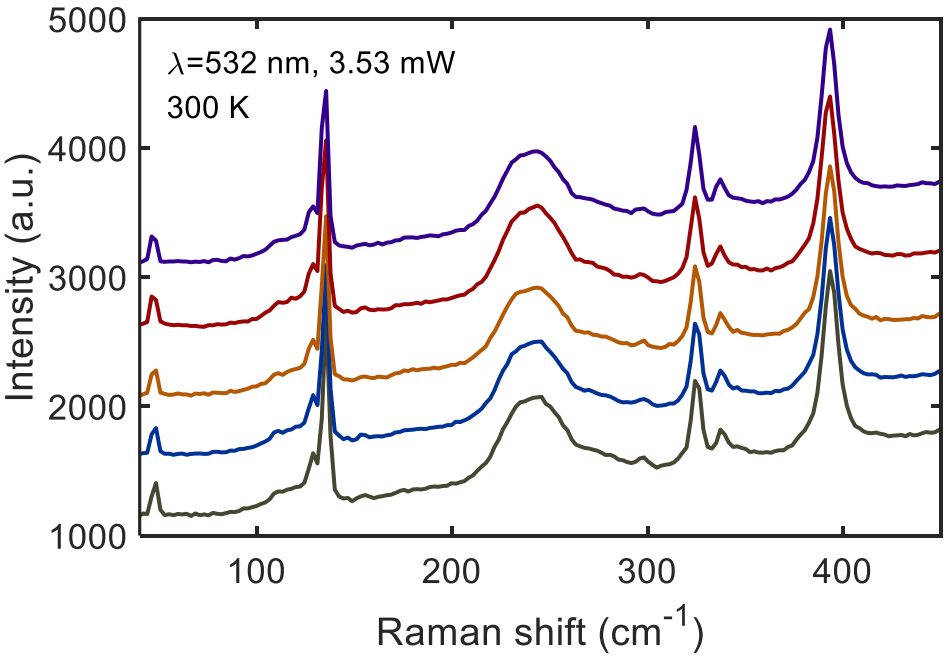

Supplementary Figure 3 | Raman spectra of $Co_{1/3}TaS_2$ at 300 K measured at five different positions in one single-crystal piece.

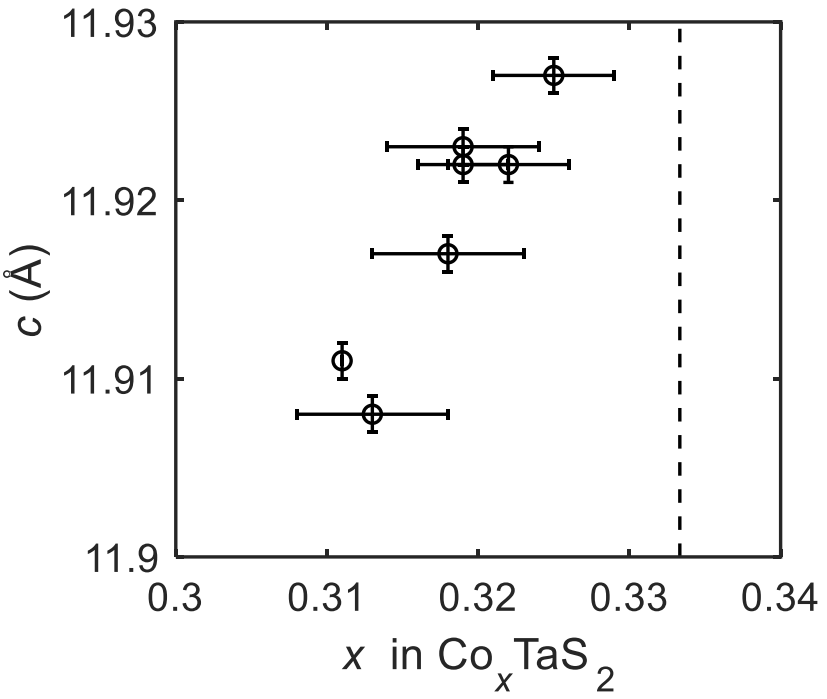

Supplementary Figure 4 | Comparison between the composition of Co (*x*) and the lattice constant *c*. The specific data are in Table S3.

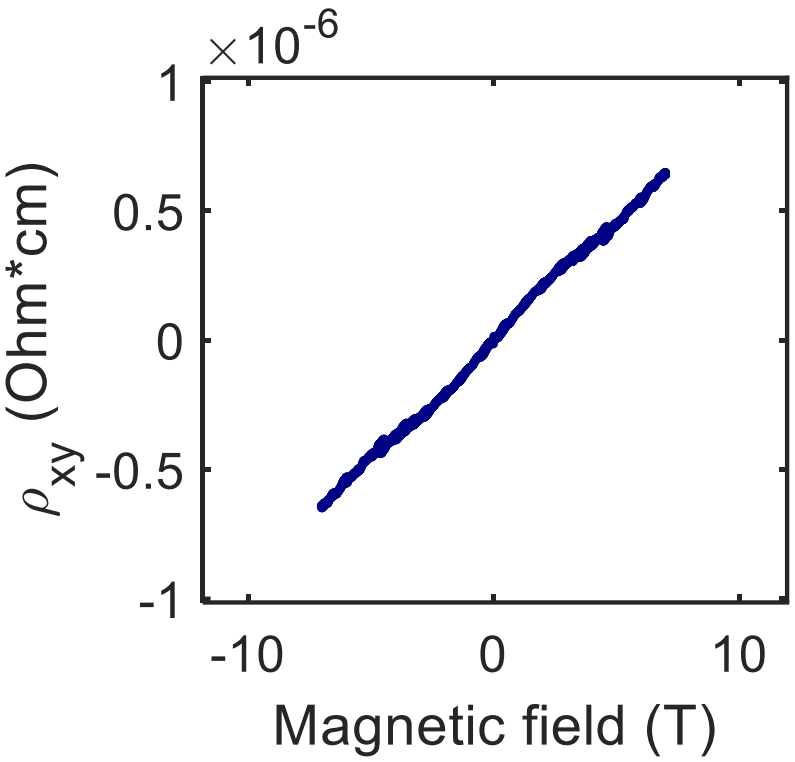

Supplementary Figure 5 | The measured field dependence of Hall resistivity ρ_{xy} at 30 K, which demonstrates the presence of metamagnetic transition when $T_{N2}<T<T_{N1}$.

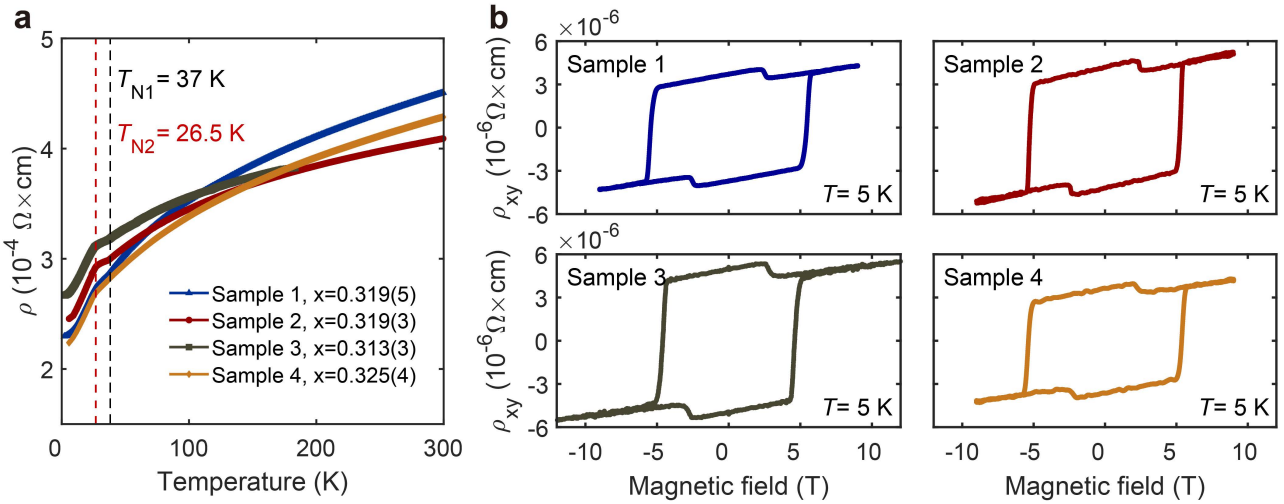

Supplementary Figure 6 | Resistivity and anomalous Hall effect in several $Co_{1/3}TaS_2$ samples. **a,** Resistivity of four $Co_{1/3}TaS_2$ samples with slightly different Co composition, which correspond to those shown in Fig. 2e. **b**, Field dependence of Hall resistivity (ρ_{xy}) in the four $Co_{1/3}TaS_2$ samples at 5 K.

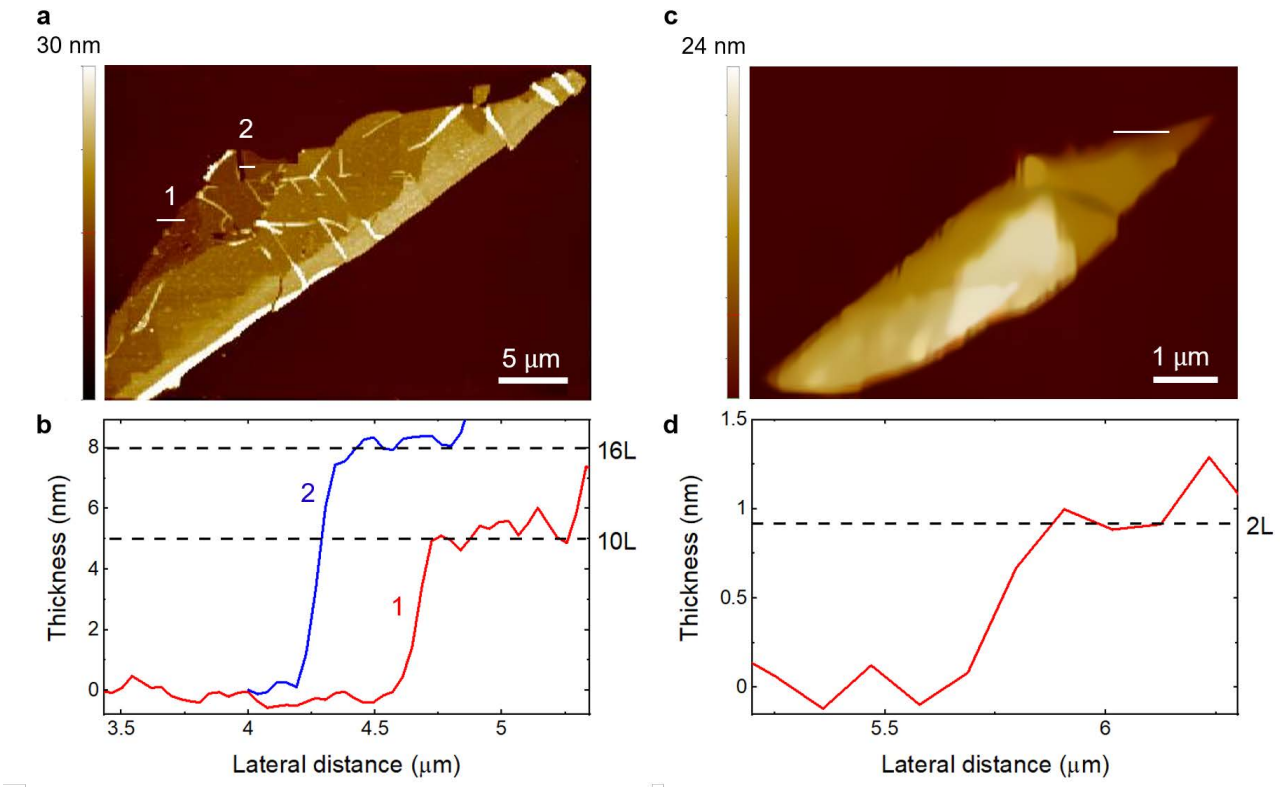

Supplementary Figure 7 | Mechanical exfoliation of $Co_{1/3}TaS_2$. a-b, AFM images of two $Co_{1/3}TaS_2$ nanoflakes exfoliated on the Au-deposited sapphire substrate. The color code shows the nanoflakes' thickness profiles. **c-d**, Thickness profiles along the white lines in **a** and **b**.

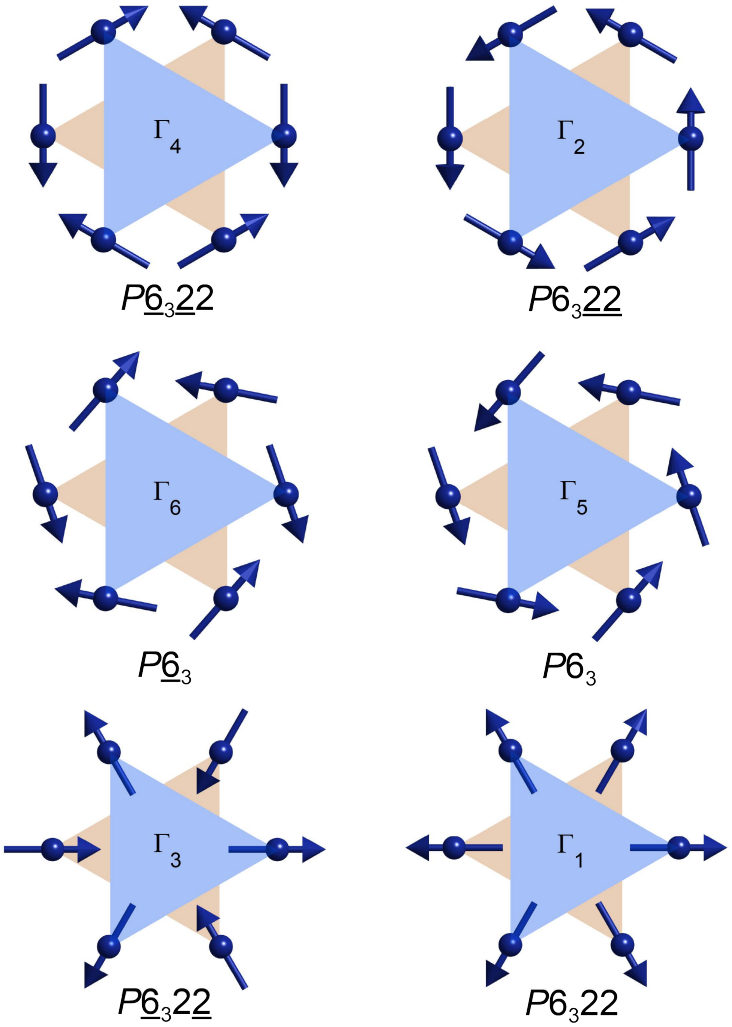

Supplementary Figure 8 | Possible noncollinear magnetic ground states of $Co_{1/3}TaS_2$ from the group representation analysis. The corresponding magnetic space group is shown below each irreducible representation, written in Hermann–Mauguin notation; symmetry operators combined with time-reversal are underlined (_) following the convention.

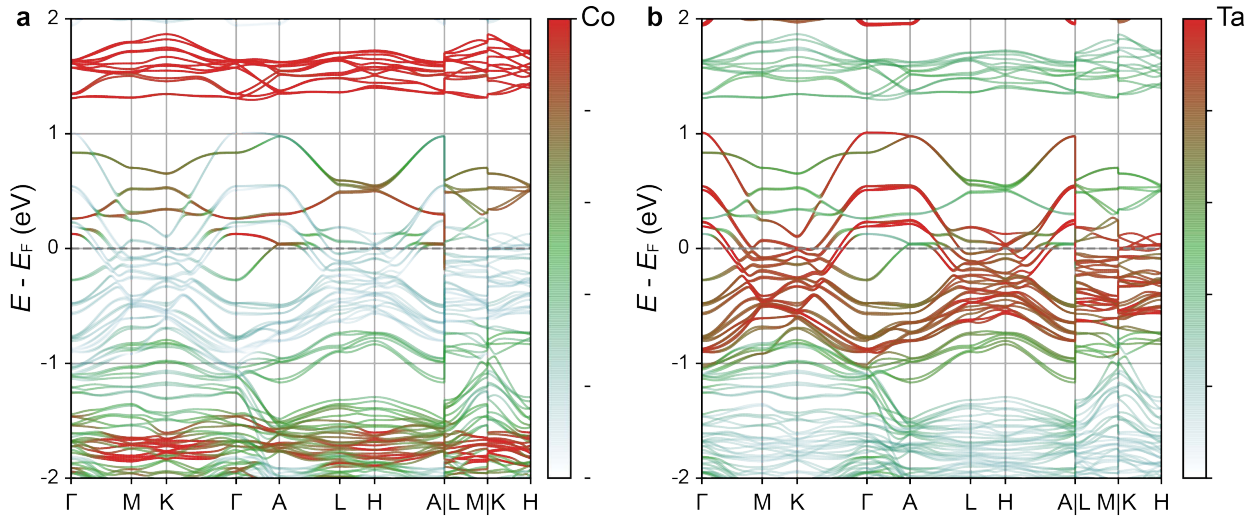

Supplementary Figure 9 | The calculated band structure of the Γ_2^+ phase in $Co_{1/3}TaS_2$. The Co-3*d* and Ta-5*d* portions are depicted by color code in **a** and **b**, respectively. The Fermi level is set at zero energy. Ta-5d orbital character dominates over the Fermi level while Co bands partly contribute.

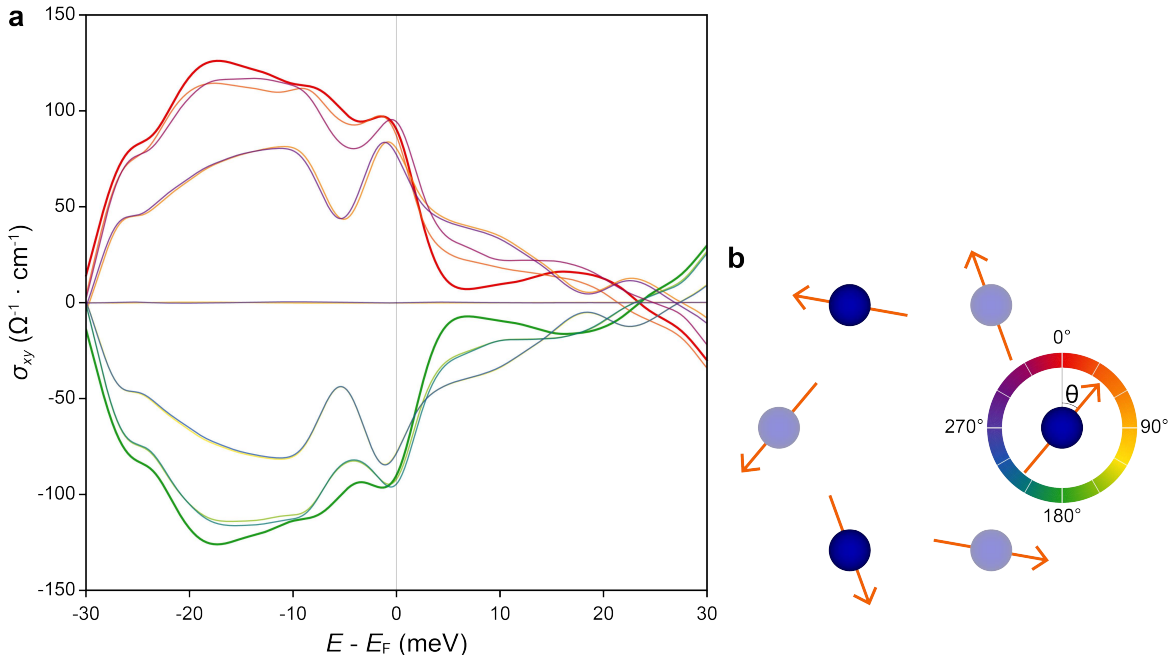

Supplementary Figure 10 | Relation between AHC and non-collinear magnetic order. a, The calculated AHC with various spin configurations. Each configuration is generated from the Γ_2^+ configuration by uniformly rotating spins about the c-axis as shown in **b**. Fermi level is set to zero energy. For $\theta = 90°$ and $270°$ (Γ_1), the in-plane C_2 rotation symmetry enforces σ_{xy}=0 through the anti-symmetry of $\Omega_z(C_2\vec{\mathbf{k}}) \rightarrow -\Omega_z(\vec{\mathbf{k}})$. The calculated AHC of θ and $\theta + 180°$ are antisymmetric as expected.

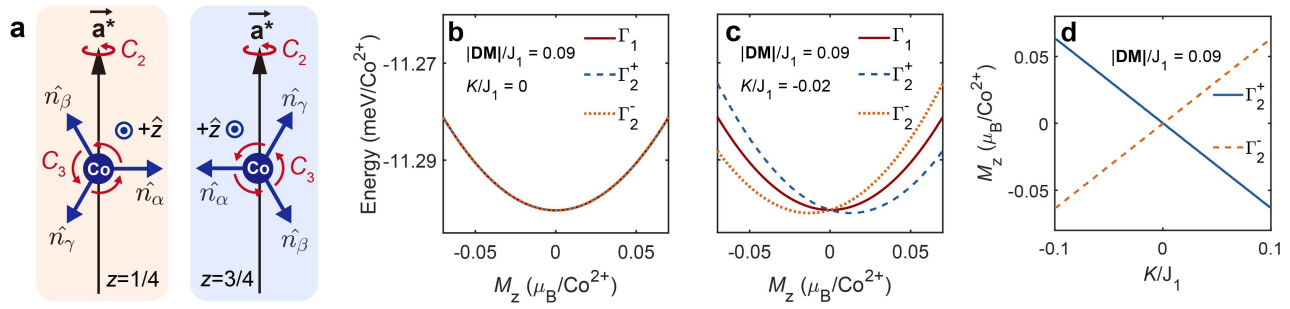

Supplementary Figure 11 | Coupling between weak ferromagnetic moments and toroidal moment in $Co_{1/3}TaS_2$. a, Symmetry operations at Co sites and local three-fold axes $\hat{\mathbf{n}}_k$ $(k = \alpha, \beta, \gamma)$ to define the higher-order on-site anisotropy (see Eq. 1). **b-c**, The calculated total energy of Γ_1, Γ_2^+ and Γ_2^- configurations without and with the on-site anisotropy as a function of magnetization along the c-axis. **d,** The weak ferromagnetic moment of Γ_2^+ and Γ_2^- configurations induced by the on-site anisotropy. We assumed that the magnitude of the DM interaction is 9 % of J_1.

Supplementary Tables

Supplementary Table 1. Refined parameters from the powder XRD pattern of $Co_{1/3}TaS_2$.

	Space group: *P* 6_3 *2 2* (No. 182) Cell dimensions: *a*=*b*=5.7374(1) Å, *c*=11.9255(1) Å, *α*=*β*=90°, *γ*=120°					
Atom	Wychoff letter	x/*a*	y/*b*	z/*c*	U_{iso} (Å^2)	Occupancy
Ta	2a	0	0	0	0.361(56)	0.1
Ta	4f	0.3333	0.6667	0.9986(1)	0.459(29)	0.2
Co	2c	0.3333	0.6667	0.25	0.701	0.0956(6)
Co	2d	0.6667	0.3333	0.25	0.308	0.0013(6)
S	12i	0.6707(9)	0.0030(7)	0.1318(1)	0.748(47)	0.6071(24)
	Agreement factors: R_p (%)=3.18, R_{wp} (%)=4.39, R_{exp} (%)=2.29, χ^2 (%)=3.67					

Supplementary Table 2. Refined parameters from the single-crystal XRD pattern of $Co_{1/3}TaS_2$.

	Space group: $P\,6_3\,2\,2$ (No. 182) Cell dimensions: a=b=5.7376(1) Å, c=11.9246(2) Å, α=β=90°, γ=120°					
Atom	Wychoff letter	x/a	y/b	z/c	U_{iso} (Å^2)	Occupancy
Ta	2a	0	0	0	0.442(7)	0.1
Ta	4f	0.3333	0.6667	0.9988(1)	0.444(7)	0.2
Co	2c	0.3333	0.6667	0.25	0.470(29)	0.1
Co	2d	0.6667	0.3333	0.25	0.308	0.002(0)
S	12i	0.6685(2)	0.0014(2)	0.1316(1)	0.476(22)	0.593(3)
	Agreement factors: R_F (%)=5.46, R_{F2} (%)=5.42, χ^2 (%)=8.25					

Supplementary Table 3. Composition (x) of Co_xTaS_2 single crystals measured by EDX spectroscopy and ICP-AES, respectively. Sample 1 ~ Sample 4 corresponds to those appearing in Fig. 2e. A lattice constant c (Å) was obtained by fitting the 2θ of (00L) Bragg peaks for the individual sample.

		EDX	ICP-AES	c (Å)
Fig. 2e	Sample 1	0.319(5)	N/A	11.923(1)
	Sample 2	0.319(3)	N/A	11.922(1)
	Sample 3	0.313(5)	N/A	11.908(1)
	Sample 4	0.325(4)	N/A	11.927(1)
Additional Samples	Sample S1	0.314(4)	0.311(0)	11.911(1)
	Sample S2	0.316(4)	0.315(0)	N/A
	Sample S3	0.322(4)	N/A	11.922(1)
	Sample S4	0.318(5)	N/A	11.917(1)

Supplementary Table 4. The sign relations between M_z, t_z and σ_{xy} in left and right chiral domains. Each pair of rows in the same color are related by a mirror (perpendicular to the a-axis). Switching the chirality flips the sign relation between t_z and M_z (σ_{xy}). The argument about M_z, t_z, and σ_{xy} in our main text is based on the right-chiral domain.

	M_z	t_z	σ_{xy}
Right-chiral	+	+	+
	-	-	-
Left-chiral	+	-	+
	-	+	-

Supplementary References

1 Parkin, S. S. P. & Friend, R. H. 3d transition-metal intercalates of the niobium and tantalum dichalcogenides. I. Magnetic properties. *Philos. Mag. B* **41**, 65-93 (1980).

2 Fan, S. *et al.* Excitations of Intercalated Metal Monolayers in Transition Metal Dichalcogenides. *Nano Lett.* **21**, 99-106 (2021).

3 Suzuki, M. T., Koretsune, T., Ochi, M. & Arita, R. Cluster multipole theory for anomalous Hall effect in antiferromagnets. *Phys. Rev. B* **95**, 094406 (2017).

4 Ding, L. *et al.* Field-tunable toroidal moment in a chiral-lattice magnet. *arXiv preprint arXiv:2103.01360* (2021).

5 Spaldin, N. A., Fiebig, M. & Mostovoy, M. The toroidal moment in condensed-matter physics and its relation to the magnetoelectric effect. *J. Phys. Condens. Matter* **20**, 434203 (2008).

6 Du, K. *et al.* Topological spin/structure couplings in layered chiral magnet Cr1/3TaS2: The discovery of spiral magnetic superstructure. *Proc. Natl. Acad. Sci.* **118** (2021).

7 Horibe, Y. *et al.* Color theorems, chiral domain topology, and magnetic properties of Fe x TaS2. *J. Am. Chem. Soc.* **136**, 8368-8373 (2014).